BULLETIN OF THE POLISH ACADEMY OF SCIENCES
TECHNICAL SCIENCES, Vol. 65, No. 1, 2017
DOI: 10.1515/bpasts-2017-0010

$FePt_3$ nanosuspension synthesized from different precursors – a morphological comparison by SAXS, DLS and TEM

P. SARMPHIM[1], S. SOONTARANON[2], C. SIRISATHITKUL[1]*, P. HARDING[1], S. KIJAMNAJSUK[3], B. CHAYASOMBAT[3], S. PINITSOONTORN[4], and J. CHINGUNPITAK[5]

[1]Molecular Technology Research Unit, Walailak University, Nakhon Si Thammarat, Thailand
[2]Synchrotron Light Research Institute, Nakhon Ratchasima, Thailand
[3]National Metal and Materials Technology Center, Pathumthani, Thailand
[4]Integrated Nanotechnology Research Center, Khon Kaen University, Khon Kaen, Thailand
[5]School of Pharmacy, Walailak University, Nakhon Si Thammarat, Thailand

Abstract. Annealed iron-platinum (FePt) is ferromagnetic in a nanoscale regime which is necessary for energy and data storage, whereas the as-synthesized form of FePt-based nanoparticles exhibits superparamagnetism useful for biomedical applications. In this study, as-synthesized nanosuspensions from the reaction of $Pt(acac)_2$ with $Fe(acac)_3$ and $Fe(hfac)_3$ are compared. X-ray diffraction (XRD) peaks for both samples are assigned to the $FePt_3$ phase. As shown by transmission electron microscopy (TEM) and small angle X-ray scattering (SAXS), nanoparticles synthesized by using $Fe(acac)_3$ have a smaller average diameter, but larger polydispersity index and particle agglomerations. On the other hand, the nanoparticles synthesized by using $Fe(hfac)_3$ can self-assemble into a longer range of patterned monolayer. Dynamic light scattering (DLS), measuring the size of cluster of nanoparticles as well as oleic acid and oleylamine at their surface, confirms that larger agglomerations in the sample were synthesized by using $Fe(acac)_3$. In addition to the size distribution, magnetic properties were influenced by the composition of these nanoparticles.

Key words: magnetic nanosuspension, $Fe(acac)_3$, $Fe(hfac)_3$, DLS, TEM, SAXS.

1. Introduction

Monodisperse iron-platinum (FePt) nanoparticles are currently under investigations for applications in ultrahigh-density data storage [1], rare-earth-free permanent magnets [2] and biomedical purposes such as biosensing, targeted drug delivery and hyperthermia treatment [3]. To this end, the ability to control the shape, size and size distribution is critically important [4, 5]. Moreover, the homogenous assembly by attractive van der Waals force and magnetic dipole interaction in monodisperse ferromagnetic nanoparticles is required in the data storage [6, 7]. The chemical synthesis normally results in the mixed phase of $FePt_3$ with iron oxides and the annealing treatment is needed to convert the as-synthesized phase into ferromagnetic FePt [8]. Nevertheless, the as-synthesized FePt-based nanoparticles also find applications based on their superparamagnetic properties.

Various techniques have been developed to accurately characterize nanoparticle morphology. The widely used transmission electron microscopy (TEM) provides images of the particles over a specific area so its main advantage is the visual impression of the homogeneity of a given sample [9]. However, TEM has potential errors due to a small area with up to thousands of particles examined. To complement TEM, dynamic light scattering (DLS) is used as an inexpensive approach to sampling a much larger number of particles dispersed in forms of magnetic nanosuspension. For surface-modified magnetic nanoparticles, DLS measures the hydrodynamic diameter corresponding to the size of nanoparticle cluster and organic surfactant, whereas TEM detects boundaries of the individual magnetic nanoparticle [10]. The correlation between TEM and DLS information has been reported in the highly uniform superparamagnetic $CoFe_2O_4$ nanoparticles [11].

Another non-destructive technique to determine the size distribution is small angle X-ray scattering (SAXS) [12]. Its advantages are the accurate determination of nanoparticle size distributions and the discrimination between polydisperse single particle and polydisperse particle in aggregates. SAXS has been successfully used to complement TEM in probing the size distribution of several nanoparticles including Au [13], $CoPt_3$ [14] and FePt [15]. Furthermore, Fe_3O_4 and CuO nanoparticles were comparatively characterized using X-ray diffractometry (XRD), TEM, DLS and SAXS [16].

In this study, the morphology of FePt-based nanoparticles synthesized from two alternative precursors is compared by using TEM, DLS and SAXS. Iron(III) acetylacetonate ($Fe(acac)_3$) and iron(III) hexafluoroacetylacetone ($Fe(hfac)_3$) have been investigated as a replacement for highly toxic $Fe(CO)_5$. The synthetic procedure, adapted from the published method [17], replaces a N_2 glove box with an Ar Schlenk line. The heating rate in the terminal process and revolution of purified centrifugation are also reduced.

*e-mail: chitnarong.siri@gmail.com

2. Experiments

2.1. Synthesis of nanosuspension. Nanoparticles were prepared by mixing 0.2 mmol of platinum(II) acetylacetonate ($Pt(acac)_2$) with 0.24 mmol of either $Fe(acac)_3$ (Sample 1) or $Fe(hfac)_3$ (Sample 2) in a 100 mL Schlenk flask. The flask was connected with a condenser and Ar gas. The temperature controlled by an IKA thermostat coupling with a hotplate stirrer kept the heating rate initially at about 5°C/min and terminally at about 1°C/min until 250°C. The schlenk flask was evacuated and then filled with Ar for 3 times before adding dioctyl ether 20 mL. The mixture was vigorously stirred and heated up to 120°C for 20 min under Ar atmosphere. Oleic acid (1.78 mL, 5.0 mmol) and oleylamine (2.3 mL, 5.0 mmol) were injected into the reaction flask (solution change to black brown) and then the solution was heated to 200°C and dwell for 30 min. The solution was refluxed at 296°C to for 30 min. The product was then cooled to room temperature under Ar. After that, the black product was mixed with 45 mL of ethanol and then centrifuged at 5, 300 rpm for 15 min. The supernatant was discarded and the precipitate was redispersed in 20 mL of hexane in the presence of small amount (0.05 mL) of oleic acid and oleylamine. To separate large and uncoated particles, 5 mL of ethanol was added, and the mixture was centrifuged at 5, 300 rpm for 15 min. The precipitate (large particles) was discarded and an excessive ethanol was added to the black suspension followed with centrifugation to precipitate the nanoparticles. The nanoparticles were further purified by redisposed in 20 mL of hexane and centrifuged with excessive ethanol (20 mL) for three times. The final precipitate was redispersed in 10 mL of hexane and small amounts (0.05 mL) of oleic acid and oleylamine, followed by purging Ar to remove O_2. The obtained suspensions were stored in glass bottles in refrigeration.

2.2. Characterization of nanoparticles. In the characterization of nanosuspensions, the particle size distribution and zeta potential measurement were carried out by using Malvern Zetasizer Nano-ZS. Each diluted nanosuspension (ph 5) was filled in a cell glass cuvette (1 mL) and DLS was then performed at room temperature to determine the hydrodynamic diameter and size distribution. Electrophoretic mobility was also measured in the same apparatus and the data were subsequently transformed to the zeta potential value which can be related to the surface charge density.

The SAXS was measured at BL1.3W of Synchrotron Light Research Institute (Public organization), Nakhon Ratchasima, Thailand. The X-ray energy used was 8 keV. The samples, contained in a liquid cell with Kapton windows, were installed in the sample holder and measured. An empty cell and a cell injected with hexane buffer were respectively used as a reference and background. Each sample was measured with 300 second exposure time, in which the maximum recorded intensity was close to the saturation of the detector. The scattering patterns were recorded using a CCD detector (Mar SX165). The recorded patterns were normalized with an integrated incident beam intensity measured by an ionization chamber. The sample transmissions were corrected using the measured beam intensity after the sample from a photodiode installed in front of the beam stop, with the empty cell used as a reference. Alignment of the measured SAXS patterns and calibration of the sample-detector distances of 1469.7 mm were performed using the measured diffraction ring of silver behenate powder. The SAXS profile for each sample was then obtained after background subtraction and circular averaging. The obtained profiles were fitted with Beaucage's model according to the unified exponential power law [18].

Before XRD and TEM characterizations, nanosuspensions were dropped on solid substrates and left overnight at room temperature for hexane evaporation. Nanoparticles were imaged by a TEM (JEOL, JEM-2010) at an accelerating voltage of 200 kV and the phases were characterized by selected-area electron diffraction (SAED) in TEM and XRD using Rigaku TTRAX III at 15 kW. Magnetic properties were measured at room temperature by means of vibrating sample magnetometry (VSM) under the magnetic field (H) between –10 and 10 kOe.

3. Results and discussion

In Fig. 1, XRD peaks of both samples are assigned to (111), (200), (220), (311) planes of the $FePt_3$ phase with face-centered cubic (fcc) structure (ICDD Ref: 001–089–2050). These peaks can be fitted to the Gaussian distribution. The shift to lower angles than those of the reference, implying the co-existence of another phase, is specially marked in the case of Sample 2. The lattice parameter (a) in Table 1 is around 3.9 A° for both samples, slightly higher than 3.8720 A° of the $FePt_3$ reference. It must be mentioned that the characteristic $FePt_3$ peaks are close to those of FePt and the lattice parameter of fcc FePt phase (ICDD Ref: 03–065–9122) is 3.841 A°. The SAED in TEM was then additionally used to confirm the phase of the nanoparticles.

The SAED patterns in Fig. 2 are matched with the characteristic (111), (200), (220), (311) planes of $FePt_3$. This $FePt_3$ phase is favored in the case of larger elemental composition of

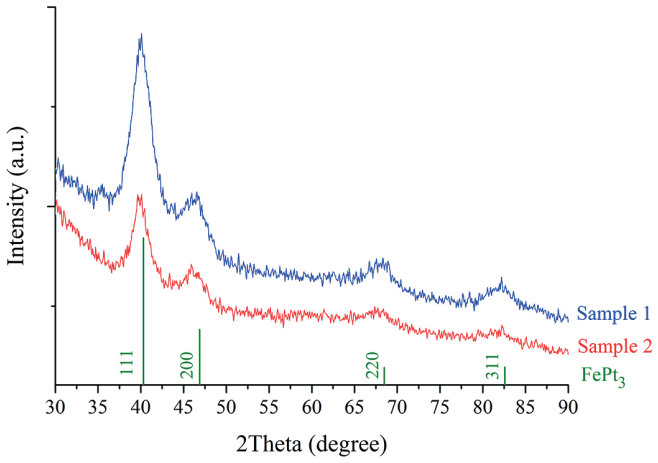

Fig. 1. XRD patterns of Samples 1 and 2

Pt. While iron oxide peaks are not present in both XRD patterns, other phases are not entirely ruled out since another set of low intensity SAED pattern, which is not matched with the $FePt_3$ phase, is superimposed on the pattern.

Table 1
XRD parameters of Samples 1 and 2 compared to the $FePt_3$ reference (ICDD Ref: 01-089-2025)

$FePt_3$			Sample 1			Sample 2		
2Theta (degree)	Int. (%)	hkl	2Theta (degree)	Int. (count)	a (A°)	2Theta (degree)	Int. (count)	a (A°)
40.31	100	111	41.02	1703	3.897	39.85	962	3.914
46.89	45.6	200	45.81	486	3.960	45.76	636	3.960
68.48	22.9	220	67.55	673	3.932	66.73	437	3.960
82.58	23.2	311	81.66	561	3.914	81.16	355	3.914

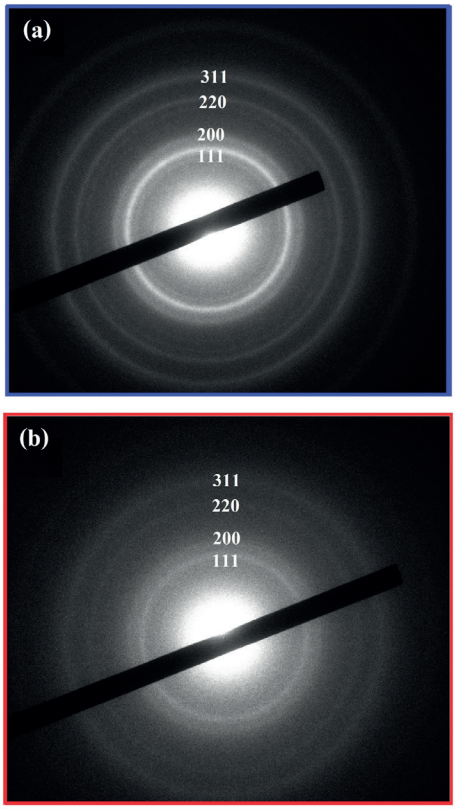

Fig. 2. SAED patterns of Samples (a) 1 and (b) 2

By applying the Image J program on over one thousand particles of each TEM image in Fig. 3, the size distribution is obtained and approximated as LogNormal curves shown in Fig. 4. From Table 2, the average diameters are 3.7±0.7 nm for Sample 1 and 4.3±0.2 nm for Sample 2. By measuring in forms of magnetic nanosuspensions, the SAXS intensity (I) plots against q in Fig. 5 exhibit a certain slope in the high q region and then a transition of profile at small q. The measured SAXS data is

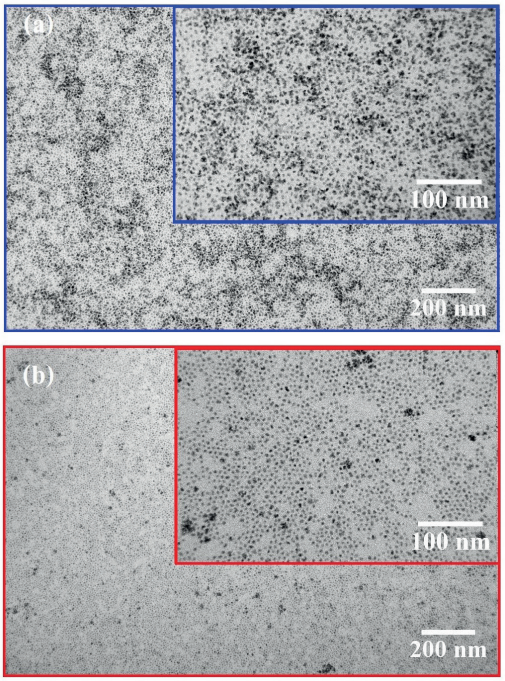

Fig. 3. TEM images of Samples (a) 1 and (b) 2 with magnified insets

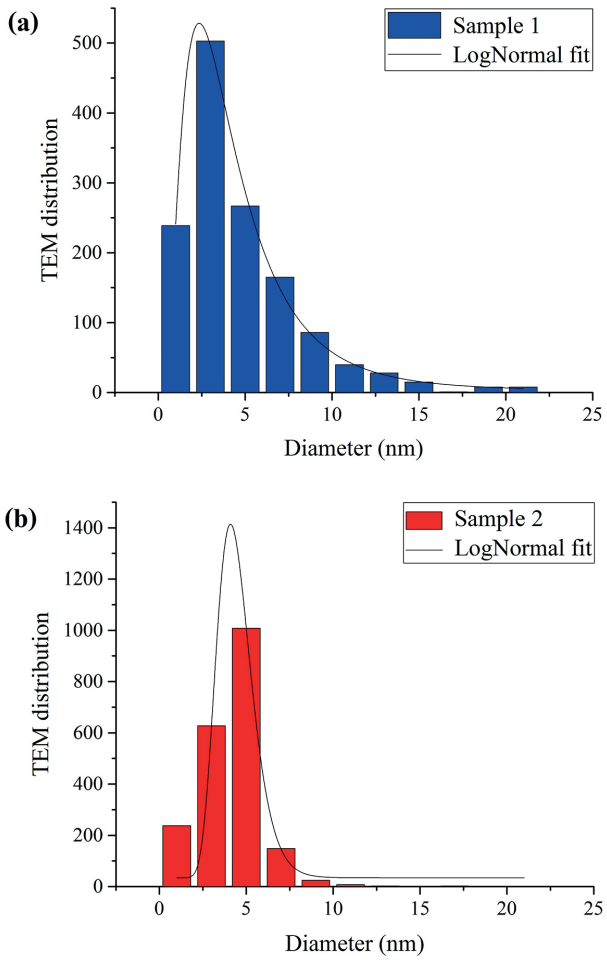

Fig. 4. Size distributions in terms of particle diameter of Samples (a) 1 and (b) 2 obtained from TEM images

Table 2
Average particle diameter (d_{av}) obtained from TEM and SAXS with hydrodynamic diameter (Hd_{av}) measured by DLS of Samples 1 and 2. Their polydispersity index (PDI) and zeta potential are also shown

Sample	TEM		SAXS		DLS		Zeta Potential (mV)
	D_{av}(nm)	PDI	D_{av}(nm)	PDI	Hd_{av}(nm)	PDI	
1	3.7	0.182	6.4	16.58	27.8	0.283	–0.91
2	4.3	0.055	10.4	4.77	16.7	0.164	7.28

fitted using the two size limit for the exponential-power scattering model of Beaucage [18, 19].

$$I(q) = Gexp\left(-\frac{q^2R_g^2}{3}\right) + Bexp\left(-\frac{q^2R_{sub}^2}{3}\right)\left\{\frac{\left[erf\left(\frac{qR_g}{\sqrt{6}}\right)\right]^3}{q}\right\}^P + \\ + G_s exp\left(-\frac{q^2R_s^2}{3}\right) + B_s\left\{\frac{\left[erf\left(\frac{qR_g}{\sqrt{6}}\right)\right]^3}{q}\right\}^{P_s} \quad (1)$$

where G and G_s are the Guinier prefactors of the larger and smaller structure. P and P_s are scaling exponent of the power law for larger and smaller structures. B and B_s are the power law prefactor of the exponent P and P_s. R_g and R_s are larger and smaller scales for radius of gyration. R_{sub} is the surface fractal cut-off radius of gyration. The first term in (1) describes the large scale of size R_g composed of small subunits of size R_s, captured in the third term. The second term describes the mass-fractal regime with two structural limits. The final two terms are the sub-structural per unit [20].

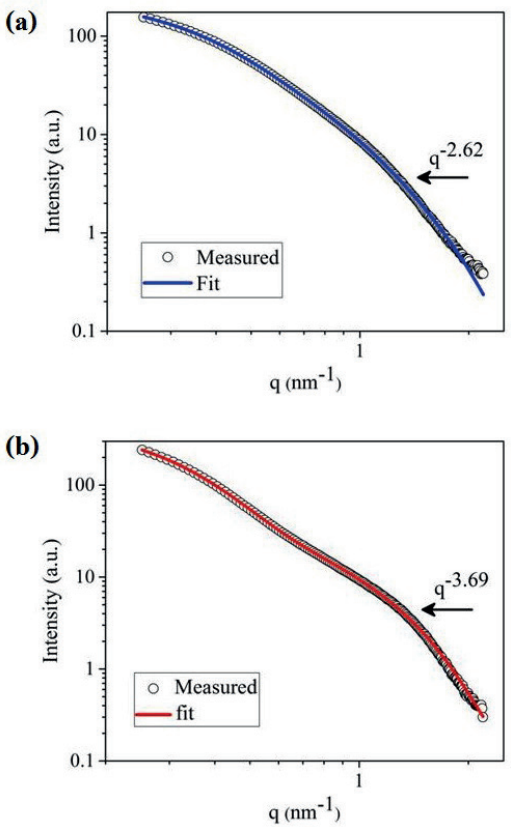

Fig. 5. SAXS profiles of Samples (a) 1 and (b) 2 measured in forms of nanosuspension. Fitted lines follow the Beaucage model

According to the fitted scattering-intensity lines shown in Fig. 5 and the values of fitting parameters listed in Table 3, Sample 1 can be fitted by the first and second terms but Sample 2 has to include the third term. For Sample 2, the second structure levels are observed in knees of the log-log plot in $1 < q < 2$ nm^{-1} regime and the fourth term will be effected by a higher existing q measured data of Sample 2. Also, there may be contribution from the last two terms unused in Sample 1.

Table 3
Beaucage fitting parameters from SAXS profiles of Samples 1 and 2

Sample	G	B	G_s	R_g (nm)	R_{sub} (nm)	R_s (nm)	P
1	248.28	13.22	0	4.73	1.11	0	2.62
2	455.59	3.09	17.40	5.81	0.01	1.74	3.69

The R_g at the low q of Sample 1 4.7 nm is less than that of Sample 2 (5.8 nm). In addition, the power law scattering at high q of Sample 2 decay with a slope of 3.69. The value close to 4 indicates the scattering from objects like polydisperse spheres. By contrast, the scattering of Sample 1 decays with a slope of 2.62 attributable to the mass-fractal structure of aggregates [19, 21].

The particle size and size distribution have been calculated assuming polydisperse spheres with a log normal distribution of radii represented by a density function $f(R)$ [22].

$$f(R) = \frac{1}{R\sigma\sqrt{2\pi}} exp\left\{\frac{[ln(R/m)]^2}{2\sigma^2}\right\} \quad (2)$$

where R is the particle radius. m is the median radius and σ is parameter of distribution related to the mean and median values. The mean particle radius $<R>$ is given as;

$$< R >= m \exp\left(\frac{\sigma^2}{2}\right) \quad (3)$$

The m and σ value of $f(R)$ can be evaluated from the model of Beaucage fitting parameters obtained from the corresponding scattering data [21].

$$m = \sqrt{\frac{5R_g^2}{3\exp(14\sigma^2)}} \quad (4)$$

$$\sigma = \sqrt{\frac{\ln\left(\frac{BR_g^4}{1.62G}\right)}{12}} \quad (5)$$

The value $\frac{BR_g^4}{1.62G}$ in eq. (5) is the polydispersity index (PDI). For monodisperse spheres, the PDI value is 1.

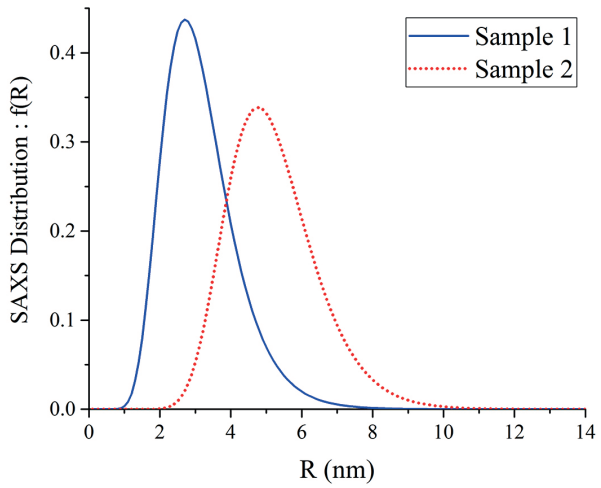

Fig. 6. Size distribution in terms of particle radius (R) of Samples (a) 1 and (b) 2 obtained from SAXS

The lognormal distribution curves are shown in Fig. 6 and the parameters obtained from SAXS are compared to other techniques in Table 2. SAXS results suggest a nearly monodispersity for larger nanoparticles synthesized by using $Fe(hfac)_3$ in Sample 2 and large polydispersity for smaller nanoparticles synthesized by using $Fe(acac)_3$ in Sample 1. These findings are in good agreement with the observation from TEM. However, the average diameters from SAXS are much higher, i.e. 6.4 nm for Sample 1 and 10.4 nm for Sample 2. The discrepancy is likely due to the deviation of particle shape from sphere used in the model.

The size distribution curves measured by DLS shown in Fig. 7 and the relevant parameters listed in Table 2 confirm the smaller PDI of Sample 2, previously indicated by TEM an SAXS. Sample 1 exhibits bimodal peaks centered at 29 and 246 nm. The hydrodynamic diameters obtained from DLS are much larger than diameters measured by TEM and SAXS. By inclusion of the organic surfactants and measuring cluster of nanoparticles, the average hydrodynamic diameters are respectively 28 and 17 nm for Samples 1 and 2.

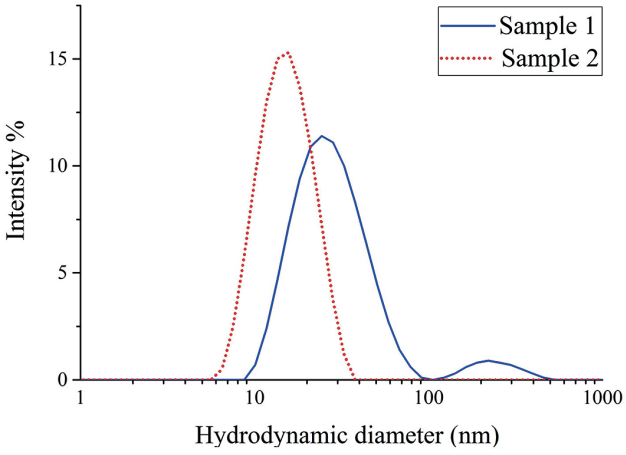

Fig. 7. Size distribution in terms of hydrodynamic diameter of Samples 1 and 2 measured by DLS

The lower PDI in Sample 2 promotes the self-assembly of uniform nanoparticles into a longer range of patterned monolayer. Sample 1 has a larger variation in size and agglomerations of some nanoparticles are clearly observed in the TEM image. The agglomeration can be quantitatively compared using TEM analysis by Image J program. Aggregates of larger than 10 nm contribute to 5.07% in Sample 1 but only 0.29% in Sample 2 which corresponding to the results from DLS. The agglomeration and self-assembly behavior can be related to the zeta potential. As shown in Table 2, the modest values well within the ±30 mV range indicate low surface charge density. The difference in zeta potential between two samples suggests that nanoparticles in Sample 1 (–0.908 mV) is likely to aggregate because of a lower repulsion. A larger potential in Sample 2 (7.28 mV) stabilizes the suspension by preventing such agglomeration.

In Fig. 8, magnetic properties of Samples 1 and 2 are compared. Without hysteresis, both samples exhibit superparamagnetic characteristics. A much smaller magnetization (M) in the case of $Fe(hfac)_3$ is consistent with the report from different set of samples in [17]. Such trend is largely attributed to the composition of nanoparticles. The synthesis with $Fe(hfac)_3$ tends to lower the Fe:Pt ratio [17].

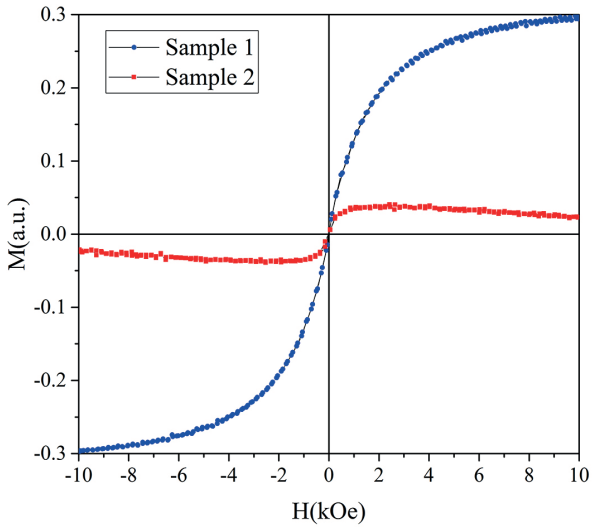

Fig. 8. Magnetic properties of Samples 1 and 2 measured by VSM

Finally, the conversion from superparamagnetism to ferromagnetism upon thermal treatments is discussed. In addition to required magnetic properties, excessive agglomerations have to be inhibited. It was demonstrated in [8] that hysteresis loops were substantially different when nanoparticles were synthesized with four different precursors. The coercive field was at the lowest in the case of $Fe(hfac)_3$ which can be traced back to its magnetic properties in the as-synthesized form.

4. Conclusions

Based on the comparative characterizations by XRD, TEM, SAXS and DLS, $Fe(hfac)_3$ shows a potential as an alternative precursor in the synthesis of monodisperse FePt nanoparticles. Although the uses of $Fe(acac)_3$, $Fe(hfac)_3$ both lead to the formation of $FePt_3$ in as-synthesized particles, the uniform size and shape are obtained by using $Fe(hfac)_3$. By contrast, the agglomeration of nanoparticles in the case of $Fe(acac)_3$ severely affects their long-range self-assembly. Judging by these morphology and self-assembly characteristics, $Fe(hfac)_3$ is a promising candidate in the synthesis of monodisperse nanoparticles. Required magnetic properties can be obtained by controlling the composition in the synthesis.

Acknowledgements. This work is financially supported by Walailak University (Annual Government Budget Grant number WU58123). The authors would like to thank P. Pinsrithong of Scientific Equipment Center, Prince of Songkla University for the assistance in TEM imaging.

References

[1] P. Wang, "FePt magnetic nanoparticles and their assembly for future magnetic media", *Proceedings of IEEE* 96, 1847–1863 (2008).

[2] O. Crisan, A.D. Crisan, I. Mercioniu, R. Nicula, and F. Vasiliu, "Development and structural characterization of exchange-spring-like nanomagnets in (Fe, Co)-Pt bulk nanocrystalline alloys", *J. Magn. Magn. Mater.* 401, 711–715 (2016).

[3] Y. Shi, M. Lin, X. Jiang, and S. Liang, "Recent advances in FePt nanoparticles for biomedicine", *J. Nanomater.* 2015, 467873 (2015).

[4] V. Nandwana, K. E. Elkins, N. Poudyal, G. S. Chaubey, K. Yano, and J. P. Liu, "Size and shape control of monodisperse FePt nanoparticles", *J. Phys. Chem. C* 111, 4185–4189 (2007).

[5] M. Farahmandjou, "Comparison of the Fe and Pt nanoparticles with FePt alloy prepared by polyol process: Shape and composition study", *Acta Phys. Pol. A* 123, 277–278 (2013).

[6] Y. Wang, M. Yang, B. Xu, Z. Yang, N. Hu, L. Wei, B. Cai, and Y. Zhang, "Controlled assembly of FePt nanoparticles monolayer on solid substrates", *J. Colloid Interf. Sci.* 417, 100–108 (2014).

[7] Y. Xia, T. D. Nguyen, M. Yang, B. Lee, A. Santos, P. Podsiadlo, Z. Tang, S. C. Glotzer, and N. A. Kotov, "Self-assembly of self-limiting monodisperse supraparticles from polydisperse nanoparticles", *Nature Nanotechnol.* 6, 580–587 (2011).

[8] W. Tangwatanakul, K. Chokprasombat, C. Sirisathitkul, P. Jantaratana, and Y. Sirisathitkul, "Magnetic phase transition of annealed FePt based nanoparticles", *J. Alloys Compd.* 654, 234–239 (2016).

[9] W. Neumann, H. Kirmse, I. Häusler, A. Mogilatenko, C. Zheng, and W. Hetaba, "Advanced microstructure diagnostics and interface analysis of modern materials by high-resolution analytical transmission electron microscopy", *Bull. Pol. Ac.: Tech.* 58, 237–253 (2010).

[10] J. K. Lim, S. P. Yeap, H. X. Che, and S. C. Low, "Characterization of magnetic nanoparticle by dynamic light scattering", *Nanoscale Res. Lett.* 8, 381 (2013).

[11] R. De Palma, S. Peeters, M. J. Van Bael, H. Van den Rul, K. Bonroy, W. Laureyn, J. Mullens, G. Borghs, and G. Maes, "Silane ligand exchange to make hydrophobic superparamagnetic nanoparticles water-dispersible", *Chem. Mater*. 19, 1821–1831 (2007).

[12] T. Rieker, A. Hanprasopwattana, A. Datye, and P. Hubbard, "Particle size distribution inferred from small-angle X-ray scattering and transmission electron microscopy", *Langmuir* 15, 638–641 (1999).

[13] M. Murawska, A. Skrzypczak, and M. Kozak, "Structure and morphology of gold nanoparticles in solution studied by TEM, SAXS and UV_Vis", *Acta Phys. Pol. A* 121, 888–892 (2012).

[14] H. Borchert, E.V. Shevehenko, A. Robert, I. Mekis, A. Kornowski, G. Grubel, and H. Weller, "Determination of nanocrystal sizes: A comparison of TEM, SAXS, and XRD studies of highly monodisperse $CoPt_3$ particles", *Langmuir* 21, 1931–1936 (2005).

[15] K. Chokprasombat, K. Koyvanich, C. Sirisathitkul, P. Harding, and S. Rugmai, "Investigation of surfactant effect on size distribution of FePt-based nanoparticles by synchrotron SAXS and TEM", *Trans Ind. Inst. Met.* 69, 733–740 (2016).

[16] S. Gopinath, and J. Philip, "Preparation of metal oxide nanoparticles of different sizes and morphologies, their characterization using small angle X-ray scattering and study of thermal properties", *Mater. Chem. Phys*. 145, 213–221(2014).

[17] K. Chokprasombat, P. Harding, C. Sirisathitkul, W. Tangwatanakul, S. Pinitsoontorn, and P. Muneesawang, "Substituent effect of Fe(β-diketonate)$_3$ on the control of self-assembly FePt-based nanoparticles", *J. Nanopart. Res.*16, 2436 (2014).

[18] G. Beaucage, "Approximations leading to a unified exponential/power-law approach to small-angle scattering", *J. Appl. Cryst*. 28, 717–728 (1995).

[19] G. Beaucage, and D. W. Schaefer, "Structural studies of complex systems using small-angle scattering: A unified Guinier/power-law approach", *J. Non-Cryst. Solids*. 172–174 , 797–805 (1994).

[20] J. Kohlbrecher, "A program for fitting elementary structure models of small angle scattering data", Paul Scherrer Institute, https://kur.web.psi.ch/sans1/SANSSoft/sasfit.pdf (2014).

[21] D. W. Schaefer, and R. S. Justice, "How nano are nanocomposites?", *Macromolecules* 40, 8501- (2007).

[22] G. Beaucage, H. K. Kammler, and S. E. Pratsinis, "Particle size distributions from small-angle scattering using global scattering functions", *J. Appl. Cryst*. 37, 523–535 (2004).